A Bayesian optimization framework for the control of combustion instability of a bluff-body stabilized combustor ⊘

Jun Yang (杨军) ⓘ ; Changxiao Shao (邵长孝) ✉ ⓘ ; Lei Wang (王磊); Qizhe Wen (文启哲); Niewei Yang (杨聂维); Zhi X. Chen (陈帜) ⓘ ; Lei Li (李磊) ⓘ ; Qiang An (安强) ⓘ ; Tai Jin (金台) ⓘ ; Kun Luo (罗坤) ⓘ

View Online   Export Citation

Articles You May Be Interested In

On the emergence of critical regions at the onset of thermoacoustic instability in a turbulent combustor

Chaos (June 2018)

Lagrangian analysis of intermittent sound sources in the flow-field of a bluff-body stabilized combustor

Physics of Fluids (February 2019)

Pressure gradient effect on flame–vortex interaction in lean premixed bluff body stabilized flames

Physics of Fluids (April 2023)

A Bayesian optimization framework for the control of combustion instability of a bluff-body stabilized combustor

Jun Yang (杨军),[1] Changxiao Shao (邵长孝),[1,a] Lei Wang (王磊),[1] Qizhe Wen (文启哲),[2] Niewei Yang (杨聂维),[3] Zhi X. Chen (陈帜),[2,4] Lei Li (李磊),[3] Qiang An (安强),[3] Tai Jin (金台),[5] and Kun Luo (罗坤)[6]

AFFILIATIONS

[1] School of Mechanical Engineering and Automation, Harbin Institute of Technology, Shenzhen 518055, People's Republic of China
[2] AI for Science Institute (AISI), Beijing 100080, People's Republic of China
[3] Research Institute of Aero-Engine, Beihang University, Beijing 100191, People's Republic of China
[4] State Key Laboratory of Turbulence and Complex Systems, Aeronautics and Astronautics, College of Engineering, Peking University, Beijing 100871, People's Republic of China
[5] School of Aeronautics and Astronautics, Zhejiang University, Hangzhou 310027, People's Republic of China
[6] State Key Laboratory of Clean Energy Utilization, Zhejiang University, Hangzhou 310027, People's Republic of China

[a] Author to whom correspondence should be addressed: shaochangxiao@hit.edu.cn

ABSTRACT

Control of combustion instability for a realistic gas-turbine combustor is challenging. This work aims to establish an efficient numerical framework for optimization to improve the combustion stability of a bluff-body combustor. Large eddy simulations of the spray combustion process are conducted, and the experimental measurements are used to evaluate the numerical accuracy of the baseline case. The air preheating temperature, the Sauter mean diameter of fuel droplets, and the location of liquid fuel injection are regarded as input variables. The root mean square of pressure amplitude is regarded as an optimization objective. The Bayesian optimization framework is proposed that includes the sampling process, surrogate model, acquisition function, and genetic algorithm optimizer processes. It is found that P_{RMS} can be reduced by 64% for the optimized case compared to the baseline case using only 17 sample evaluations. This work is promising as it provides an effective optimization framework for the development of next-generation gas-turbine combustors.

Published under an exclusive license by AIP Publishing. https://doi.org/10.1063/5.0207790

I. INTRODUCTION

The design of modern gas-turbine combustors should simultaneously consider combustion efficiency, emission reduction, safety, and turbine durability. To achieve these goals, optimization approaches are employed within the combustor design process. Davis and Samuelsen[1] proposed an active control methodology in conjunction with geometric articulation to establish optimal conditions for the gas-turbine combustor. They found that both combustion efficiency and emissions of oxides of nitrogen are optimized. Combustion efficiency and emission reduction were also pursued through catalyst optimization by Kyritsis et al.[2] An optimization technique that entails the use of computational fluid dynamics and mathematical optimization is used to obtain a more uniform combustor exit temperature profile by Motsamai et al.[3] A multi-fidelity surrogate modeling-based design

optimization[4] was used in the gas-turbine combustor, and the optimization cost was significantly reduced.

Combustion instability is one of the significant problems affecting safety in modern gas-turbine combustors. Temperature and pressure peaks due to combustion instability are particularly harmful for the structural damage they can cause as well as for performance degradation and increase in pollutant emissions.[5] An active combustion instability control was proposed by Seume et al.[6] A feedback system was developed that counteracts combustion instabilities by modulation of the fuel flow rate with rapid valves. It was found that a reduction of combustion-induced pressure amplitudes is achieved by 86%. An innovative neural-network-based technique[5] was proposed to suppress undesired thermoacoustic combustion instabilities, and satisfactory performance was obtained. Liu et al.[7] used linear genetic programing

22 November 2025 03:01:10

to simultaneously control combustion instabilities and NOx emissions in a lean premixed flame. They found that the pressure amplitude and NOx emissions are reduced by 67.1% and 36.9% under the optimal control law. However, all these works are experimental investigations. The control of combustion instability is still the main issue for the performance of gas-turbine combustors.

The Bayesian approach has been a promising tool for optimization and has applications in the combustion community. Bell *et al.*[8] proposed a Bayesian approach to calibrate hydrogen flame kinetics. The rate constants in the kinetic model were globally optimized by the Bayesian optimization algorithm.[9] It was found that the optimized model well predicts the laminar flame speeds and the ignition delay times. The Bayesian approach is also applied to the design of combustion kinetic experiments,[10] minimization of the uncertainty for the parameters in combustion kinetics models,[11–14] and model training.[15]

This work aims to propose a Bayesian optimization framework for the control of combustion instability of a bluff-body stabilized combustor. The remainder of this paper is organized as follows. The numerical methods are in Sec. II. The results and discussion are in Sec. III, and the conclusions are summarized in Sec. IV.

II. NUMERICAL METHODS
A. Bayesian theorem and the optimization process

Bayesian optimization aims to find the global optimum of the computationally expensive unknown objective function with as few evaluations as possible.[16] Its name comes from the "Bayesian theorem" in the probability theory, which describes how to obtain a posterior probability from observed data (prior probability).[17] In the belief of Bayesian optimization, although the exact form of the objective function is unknown, there is prior knowledge regarding certain properties of the function, such as its smoothness and continuity, which makes

certain potential objective functions more plausible compared to others.[17] Let x_i represent the i_{th} sample, and $f(x_i)$ is the value of the objective function at x_i. As the sample dataset $D_{1:n} = \{x_{1:n}, f(x_{1:n})\}$ is collected, the posterior distribution is combined with the likelihood function $P(D_{1:n}|f)$. The posterior distribution can be obtained as[17]

$$P(f|D_{1:n}) \propto P(D_{1:n}|f)P(f), \tag{1}$$

which provides a measure of uncertainty about the objective function after considering the evaluated samples. When the number of samples is sufficient, the posterior mean function will converge toward the original objective function. The Bayesian optimization framework established based on the principles described above is an iterative process.

Figure 1 shows the diagram for improving the combustion stability of the bluff-body combustor with the traditional optimization method and the Bayesian optimization method. The main difference between the two approaches lies in the interaction method between the optimizer and the computational fluid dynamics (CFD) analysis module. In the process of Bayesian optimization, the optimizer operates on the surrogate model, which predicts the value of the objective function and provides the posterior probability distribution based on the current data.[18] The CFD analysis is utilized only for a limited number of design points used for updating the surrogate model. This crucial difference enables Bayesian optimization to effectively reduce computational costs.

Additionally, as depicted in Fig. 1, an essence of Bayesian optimization lies in the selection of the acquisition function, which is a criterion function calculated from the posterior probability distribution, and is used to determine the evaluation point to iterate the surrogate model. It plays a vital role in guiding the optimization process toward the most promising regions of the designed space. Specifically, in this work, the Kriging method is utilized to establish the surrogate model,
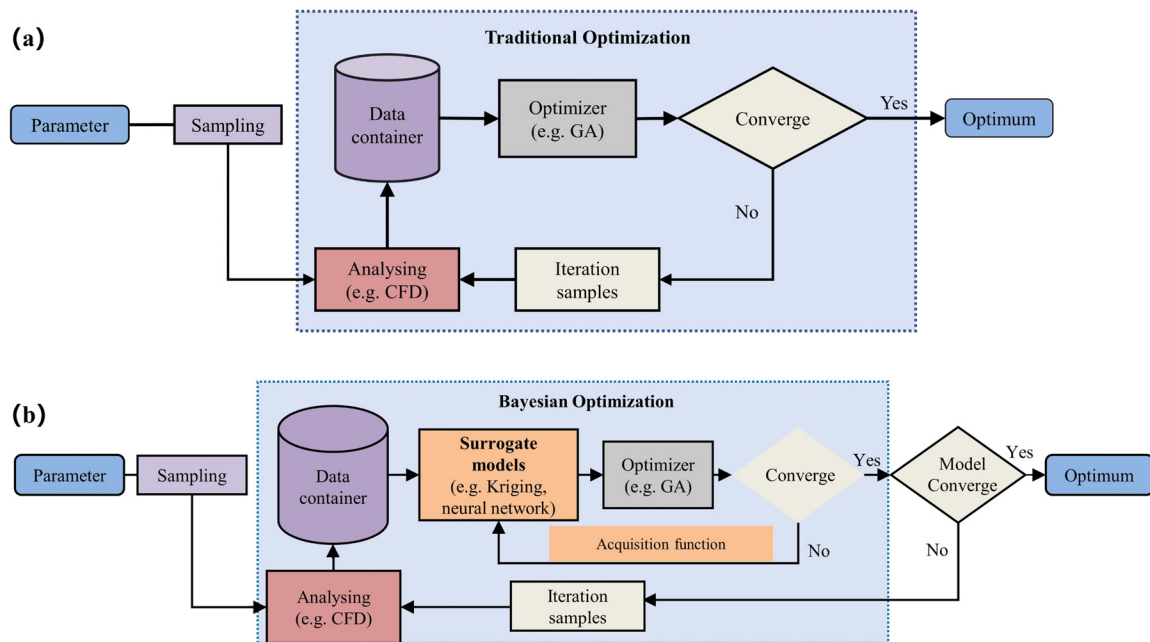
FIG. 1. Diagram for improving the combustion stability of the combustor with (a) traditional optimization method and (b) Bayesian optimization method.

while the expected improvement (EI) acquisition function is applied.[16] Furthermore, the genetic algorithm (GA) is employed as the optimizer to maximize the EI function in each iteration. The overall procedure of the Bayesian optimization can be described as follows:

1. The input variables and optimization objective are determined.
2. CFD analysis on the corresponding cases of initial sample points selected with arbitrary space-filling method is performed.
3. A surrogate model (Kriging) between the input parameters and the objective function is constructed.
4. The point with maximum EI using the GA optimizer is explored.
5. The maximum EI point as an additional sample point is added, and the corresponding CFD analysis is performed.
6. Steps 3–5 are iterated until the termination criterion (maximum number of sample points or tolerance of uncertainty) is met.

The details of each step will be introduced in the subsequent subsections.

B. Design space and optimization objectives

To tackle an optimization problem, the design space and optimization objectives should be defined in the first step. In the present work, air preheating temperature (T_{air}), location of liquid fuel injection (L_{inj}), and Sauter mean diameter (SMD) of liquid fuel are selected as design variables, which are believed to have a significant impact on the combustion instability in current research. Here, L_{inj} is the distance from the inlet to the fuel injection. SMD is an important characteristic parameter of liquid fuels related to the cumulative distribution function. The cumulative distribution function used here is the Rosin–Rammler model, which is defined as

$$F_M(x) = \frac{1 - e^{-\left(\frac{x-d_0}{d}\right)^n}}{1 - e^{-\left(\frac{d_1-d_0}{d}\right)^n}}, \quad (2)$$

where x is the diameter to be calculated, d_0 is the minimum diameter of the liquid fuels, d_1 is the maximum diameter of the liquid fuels, d is a parameter that affects the position of the symmetry axis of the distribution function, and n is a parameter that affects the aggregation level of the distribution function, which is called distribution index. SMD is expressed as follows:[19]

$$SMD = \frac{\int_{d_0}^{d_1} x^3 f_M(x) dx}{\int_{d_0}^{d_1} x^2 f_M(x) dx}, \quad (3)$$

where $f_M(x)$ is the probability density function derived from the cumulative distribution function.

Wang et al.[20] investigated the impact of droplet diameter on spray combustion. The results indicated that the droplet diameter primarily influences the evaporation rate and evaporation lifetime, with the overall premixed combustion fraction decreasing as the droplet diameter increases. Desai and Chakravarthy[21] investigated the effect of fuel injection positions downstream of a step flame stabilizer. The results demonstrated that the injection position affects the phase relationship between fuel supply and heat release of the combustor, subsequently influencing the combustion instability. Cuppoletti et al.[22] studied the effects of V-groove structures, inlet Mach numbers, and

TABLE I. The design space for the optimization process.

Input variable	Range
Sauter mean diameter (SMD)	20–100 μm
Air preheating temperature (T_{air})	800–1200 K
Location of liquid fuel injection (L_{inj})	133.8–176.2 mm

inlet temperatures on the combustion instability of a model combustor. The results revealed the presence of screech instability at lower inlet temperatures.

The design space for the optimization process is shown in Table I.

The objective of this work is to improve the combustion stability of the combustor. Specifically, the fluctuation of pressure is considered as the target performance parameter. Broda et al.[23] conducted experimental research on combustion instability and used pulse the root mean square error of pressure amplitude (P_{RMS}) to evaluate combustion instability, which is defined as

$$P_{RMS} = \sqrt{\frac{\sum_{n=1}^{N} (p_t - \bar{p})^2}{N}}, \quad (4)$$

where p_t is the time series data of pressure, $\bar{p}$ is the average pressure, and N is the data length of p'.

C. Surrogate model

The Kriging model is one of the most widely used surrogate models, characterized by strong robustness,[24] which introduces statistical assumptions that treat the unknown function as a specific realization of a Gaussian stationary random process. The stationary random process is defined as

$$\mathscr{Y}(\mathbf{x}) = \delta + \mathscr{Z}(\mathbf{x}), \quad (5)$$

where $\mathbf{x}$ is a vector in m dimension (m input variables) and δ is an unknown constant known as the global trend model, which represents the mathematical expectation of $\mathscr{Y}(\mathbf{x})$. Here, $\mathscr{Z}(\cdot)$ is a stationary random process with zero mean and variance σ^2, whose spatial covariance matrix is given by

$$\mathrm{Cov}[\mathscr{Z}(\mathbf{x}^i), \mathscr{Z}(\mathbf{x}^j)] = \sigma^2 R(\mathbf{x}^i, \mathbf{x}^j), \quad (6)$$

where $\mathbf{R}$ is the correlation matrix composed of the correlation function values between all known sample points. The correlation function used in this work is a Gaussian (square exponential) function as follows:

$$R(\mathbf{x}^i, \mathbf{x}^j) = \exp\left(-\sum_{k=1}^{m} \theta_k \left(x_k^i - x_k^j\right)^2\right), \quad \theta_k \in \mathbb{R}^+, \quad (7)$$

where θ_k is the parameter that determines how fast the correlation function "drops off" as one moves in the kth coordinate direction.

The prediction result for new design point $\mathbf{x}^*$ is

$$\widehat{y}(\mathbf{x}^*) = \widehat{\delta} + \mathbf{r}^T \mathbf{R}^{-1}(\mathbf{y_s} - \mathbf{I}\widehat{\delta}), \quad (8)$$

where $\widehat{y}$ is the prediction value of $\mathscr{Y}$, while $\mathbf{y_s}$ is the current sampling dataset (n sample points). $\mathbf{r}$ is the correlation vector that consists of the correlation function values between $\mathbf{x}^*$ and all known sample points. $\mathbf{I}$ is the identity matrix. The unknown parameters (θ_k, δ, σ^2) are

estimated in the process of maximizing the likelihood function **L**, which is expressed as follows:

$$\log(\mathbf{L}) = -\frac{n}{2}\log\left(\sigma^2\right) - \frac{1}{2}\log(|\mathbf{R}|) - \frac{(\mathbf{y_s} - \mathbf{I}\delta)^T\mathbf{R}^{-1}(\mathbf{y_s} - \mathbf{I}\delta)}{2\sigma^2}.$$

(9)

By taking partial derivatives, the likelihood function is maximized when δ and σ^2 satisfy the following expressions:

$$\widehat{\delta} = \frac{\mathbf{I}^T\mathbf{R}^{-1}\mathbf{y_s}}{\mathbf{I}^T\mathbf{R}^{-1}\mathbf{I}},$$

(10)

$$\widehat{\sigma}^2 = \frac{(\mathbf{y_s} - \mathbf{I}\widehat{\delta})^T\mathbf{R}^{-1}(\mathbf{y_s} - \mathbf{I}\widehat{\delta})}{n}.$$

(11)

Substituting the expressions of δ and σ^2 in Eq. (9), we obtain a simplified form of the likelihood function as

$$\log(\mathbf{L}) = -\frac{n}{2}\log\left(\widehat{\sigma}^2\right) - \frac{1}{2}\log(|\mathbf{R}|).$$

(12)

Here, **L** is a function of the parameter θ_k. By using the genetic algorithm to find the parameters θ_k that maximize the likelihood function **L**, the prediction results of the surrogate model can be obtained with Eq. (8). Equations (5)–(12) and detailed derivation process can be found in Ref. 24.

D. Acquisition function and optimizer

The EI criterion[26] is used to estimate the expectation of obtaining a solution superior to the current optimum. In minimization problems, the value of EI can be calculated with the posterior probability distribution provided by the Kriging model, as follows:[18]

$$I(\mathbf{x}) = \frac{y(\mathbf{x}) - \mathbf{y_s}^{opt}}{\sigma(\mathbf{x})},$$

$$EI(\mathbf{x}) = \begin{cases} \sigma(\mathbf{x})I\Phi(I) + \sigma(\mathbf{x})\phi(I), & \sigma(\mathbf{x}) > 0, \\ 0, & \sigma(\mathbf{x}) = 0, \end{cases}$$

(13)

where $\mathbf{y_s}^{opt}$ represents the optimum value in the current sampling dataset, while $y(\mathbf{x})$ and $\sigma(\mathbf{x})$ are the prediction value and variance, respectively, of the normal distribution given by the surrogate model. The function Φ denotes the cumulative distribution function of the normal distribution, and ϕ represents the probability density function of the normal distribution.

The GA, also known as the evolutionary algorithm, is one of the classical meta-heuristic algorithms based on the principles of natural selection, and genetics[27] is employed to maximize the EI acquisition function in each iteration of the Bayesian optimization process.

The main process of GA is as follows:

1. Initialize population: Some samples (individuals) from the design space to form the initial population are selected.
2. Fitness evaluation: The fitness function of all individuals in the current population is evaluated.
3. Check termination condition: If the termination condition (reaching a maximum number of iterations or achieving the desired fitness threshold) is satisfied, the iteration stops, while the optimal solution is returned.

4. Genetic operation: Operators, including selection, crossover, and mutation, are employed to generate a new population with a higher potential for finding the optimum.
5. Population update: The original individuals are replaced with the newly generated offspring individuals to form the updated population.
6. Steps 2–5 are iterated until the termination condition is satisfied.

Here, the fitness function is the current acquisition function (the EI criterion). The genetic operations include selection, crossover, and mutation.[28] In selection operation, better individuals are selected and made copies to form a mating pool, which is usually the first operator applied on a population. In crossover operation, different individuals are generated by exchanging some bits in the two chosen individuals of the previous generation, including one site crossover and two site crossover. In mutation operation, new individuals are generated by randomly changing one or several bits in an individual, ultimately helping to prevent local searches of the search space and increasing the probability of finding global optima. The probability of crossover and mutation is set to 0.9 and 0.05, respectively. After evaluating the EI function for each initial individual, the selection, crossover, and mutation are performed to generate new individuals. The initial population is set to 1000. The maximum number of iterations is set to 300. The original individuals are replaced by the newly generated offspring individuals, which is how the population is updated.

By iteratively executing these steps, the algorithm explores the design space and improves the approximation toward the optimal solution by evolving a population.[29] Due to its characteristics of not requiring gradient information of the objective function, being less prone to local optima, and being easily paralleled, the GA demonstrates robustness in achieving approximate solutions to the global optimum and has been widely applied in industrial applications.[27]

E. Numerical simulation of spray combustion in the combustor

1. Configuration and boundary conditions

Figure 2 shows the three-dimensional experimental setup of the bluff-body stabilized combustor. The experimental setup consists of two three-dimensional V-shaped bluff-bodies placed in a channel with a rectangle cross section (0.2×0.8 m^2). The test case is operated at 1 atmosphere. The air flows from the left inlet boundary in the x-direction and exits to the right outlet boundary. The physical boundaries
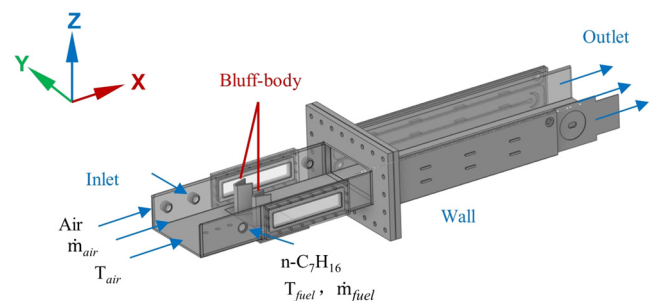

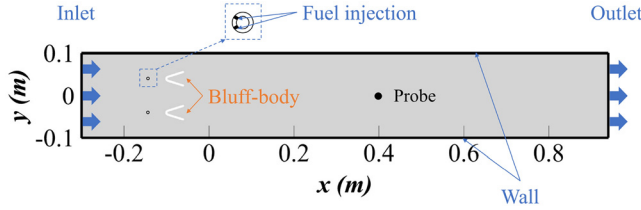**FIG. 2.** Three-dimensional experimental setup of the bluff-body stabilized combustor.

FIG. 3. Simplified two-dimensional configuration of the bluff-body stabilized combustor.

in the y and z directions are wall boundaries. The channel length is 1.24 m. The main parameters of each V-shaped bluff-body are as follows: span angle is 35°, thickness is 5 mm, blockage width is 37 mm, and length is 45 mm. In the spanwise z direction, the bluff-bodies extend from one side of the channel to the other. Hence, it can be simplified to a 2D simulation.

Figure 3 shows the 2D bluff-body geometry considered in the present study. The test section consists of a pair of 2D bluff-bodies placed in a channel with 1.24×0.2 m². The probe for pressure monitoring is located at (0.4 m, 0 m). The air inlet is specified as a velocity inlet. For the outlet boundary, a pressure outlet is used and set to one atmosphere. In addition, a nonreflecting boundary condition is applied in both inlet and outlet. Non-slip adiabatic boundary conditions are enforced on the walls. The air with a velocity of 56 m/s at 800 K is delivered from $x = 0$, and the fuel with a mass flow rate of 8.16 g/s at 320 K is injected at four locations upstream of the bluff-body. The fuel injection directions of adjacent injection points have an angle of 60°. Additionally, the droplet size distribution obeys the Rosin–Rammler distribution with the Sauter mean diameter (SMD) 60 μm. The Reynolds number is about 133 000. The mesh is refined near the bluff-body wall and consists of approximately 160 000 elements.

2. Governing equations

In this work, the large eddy simulation (LES) method is applied to deal with the Navier–Stokes equations of transient compressible flow.[30] The conservation of mass is defined as

$$\frac{\partial \overline{\rho}}{\partial t} + \nabla \cdot (\overline{\rho}\widetilde{\boldsymbol{u}}) = \overline{S}_\rho, \tag{14}$$

where $\overline{\rho}$ is the implicitly filtered density and $\widetilde{\boldsymbol{u}}$ is filtered velocity. The conservation of momentum is defined as

$$\frac{\partial(\overline{\rho}\widetilde{\boldsymbol{u}})}{\partial t} + \nabla \cdot (\overline{\rho}\widetilde{\boldsymbol{u}} \otimes \widetilde{\boldsymbol{u}}) = -\nabla\overline{p} + \nabla \cdot (\overline{\rho}\widetilde{\boldsymbol{u}} \otimes \widetilde{\boldsymbol{u}} - \overline{\rho\widetilde{\boldsymbol{u} \otimes \boldsymbol{u}}} + \overline{\sigma}) + \overline{S}_{\boldsymbol{u}}, \tag{15}$$

where $\overline{p}$ is filtered pressure, while $\overline{\sigma}$ is the viscous stress tensor.[30] The symbol ($\otimes$) refers to the outer product. The energy equation is shown as

$$\frac{\partial\left(\overline{\rho}\widetilde{h}_t\right)}{\partial t} + \nabla \cdot \left(\overline{\rho}\widetilde{\boldsymbol{u}}\widetilde{h}_t\right)$$
$$= \frac{\partial\overline{p}}{\partial t} + \nabla \cdot \left(\overline{\rho}\overline{D}\nabla\widetilde{h}_s + \widetilde{\rho}\widetilde{\boldsymbol{u}}\widetilde{h}_s - \overline{\rho}\widetilde{\boldsymbol{u}}h_s\right) + \overline{S}_h + \overline{\omega}_h, \tag{16}$$

where $\widetilde{h}_t$, $\widetilde{h}_s$ are the filtered total and sensitive enthalpy, respectively. The chemical term $\overline{\omega}_h$ denotes the heat release rate (HRR) of species i. The conservation of species mass fraction is defined as

$$\frac{\partial\left(\overline{\rho}\widetilde{Y}_k\right)}{\partial t} + \nabla \cdot \left(\overline{\rho}\widetilde{\boldsymbol{u}}\widetilde{Y}_k\right) = \nabla \cdot \left(\overline{\rho}\overline{D}\nabla\widetilde{Y}_k + \overline{\rho}\widetilde{\boldsymbol{u}}\widetilde{Y}_k - \overline{\rho}\widetilde{\boldsymbol{u}}_k\right) + \overline{S}_{Y_k} + \overline{\omega}_k, \tag{17}$$

where $\widetilde{Y}_k$ is the filtered mass fraction of species k and $\overline{D}$ is the filtered mass diffusivity. $\overline{\omega}_k$ is the filtered production rate of species i due to chemical reactions and is modeled with the Partially Stirred Reactor (PaSR) combustion model,[31] which is defined as

$$\overline{\omega}_i = \gamma^*\dot{\omega}_i^* + (1 - \gamma^*)\dot{\omega}_i^0, \tag{18}$$

where γ^* is the reacting volume fraction, $\dot{\omega}_i^*$ is the production rate in the fine structures, and ω_i^0 is the production rate in the surroundings. In the PaSR combustion model, γ^* is expressed as

$$\gamma^* = \frac{\tau_c}{\tau_c + \tau^*}, \tag{19}$$

where τ_c is the chemical timescale and τ^* is the turbulent mixing timescale. More details about the PaSR combustion model can be found in Ref. 31. Additionally, the filtered source terms $\overline{S}_\rho$, $\overline{S}_{\boldsymbol{u}}$, $\widetilde{Y}_k$, and $\overline{S}_h$ account for the liquid spray heat and mass transfer, including phase change, in the respective LES formulations.[30]

3. Physical models and numerical schemes

The solver used in this work is based on SprayFoam, which is a transient solver suitable for compressible gas–liquid two-phase spray combustion. The Euler–Lagrange method is used to simulate the spray. In the sub-model of liquid atomization, the coneInjection model is used for the fuel injection, and the force acting on droplets is the sphereDrag model. The ReitzDiwakar model is used for atomization. The liquidEvaporationBoil model is used for droplet evaporation. The PaSR model is used for the combustion model.

In order to reduce the computational cost and quickly obtain the iterative, a single-step reaction mechanism for C_7H_{16}/air combustion is considered as shown in Table II. It demonstrates good agreements with those from a skeletal n-C_7H_{16} mechanism[32] and has been used for modeling spray combustion.[25,33]

The Wale model is selected as the sub-grid-scale model. Although the Smagorinsky model is the most widely used LES model at present, which can combine the van Driest function to correct the turbulent viscosity close to the wall, it requires much more grid points
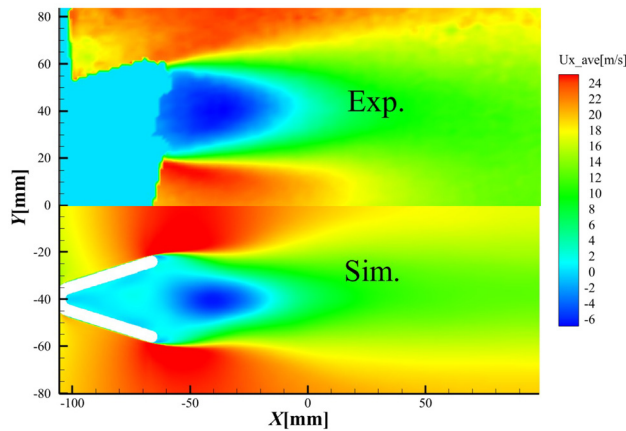
TABLE II. Single-step reaction mechanism of C_7H_{16}/air combustion and parameters.[25] A is the pre-exponential factor, n is the temperature exponent, E_a is the activation energy, and a and b are the fuel and oxidizer reaction orders, respectively.

Reaction	A [m³/(kmol s)]	n	E_a (J/kmol)	a	b
$2n - C_7H_{16} + 15O_2 \Rightarrow 14CO_2 + 16H_2O$	2.87×10^9	0	1.25×10^8	0.25	1.5

FIG. 4. The comparison of the time-averaged axial velocity field between the experimental result at the upper panel and the simulation result at the lower panel.

to form a boundary layer. Compared to the Smagorinsky model, the Wale model is easier to use and the computation is more stable.

The governing equations and boundary conditions are solved numerically using a density-based, finite-volume methodology. The

pressure–velocity coupling is solved by the PIMPLE method to ensure accurate and efficient convergence, which is the combination of the SIMPLE method and the PISO method. The temporal term is discretized using the first-order implicit Euler scheme. The gradient term, the convection term, and the diffusion term are discretized using the second-order central difference scheme. Multi-block domain decomposition is used to facilitate the implementation of parallel computation.

III. RESULTS AND DISCUSSION
A. Combustion characteristics of the baseline case

Measured and computational time-averaged axial velocity fields in the vicinity of bluff-body are compared in Fig. 4. Particle image velocimetry (PIV) is applied in the experimental measurement. The coordinate origin is located 60 mm downstream of the bluff-body tail. The axial velocity exhibits a good overall agreement. The main characteristic of the flow field is the occurrence of the recirculation zone after the bluff-body. The velocity increases between the bluff-bodies and near the walls due to the smaller cross section. Quantitatively, the time-averaged and RMS axial and radial velocities between the experimental measurements (denoted as dots) and the simulation results (denoted as lines) are compared in Fig. 5. It shows that the simulation
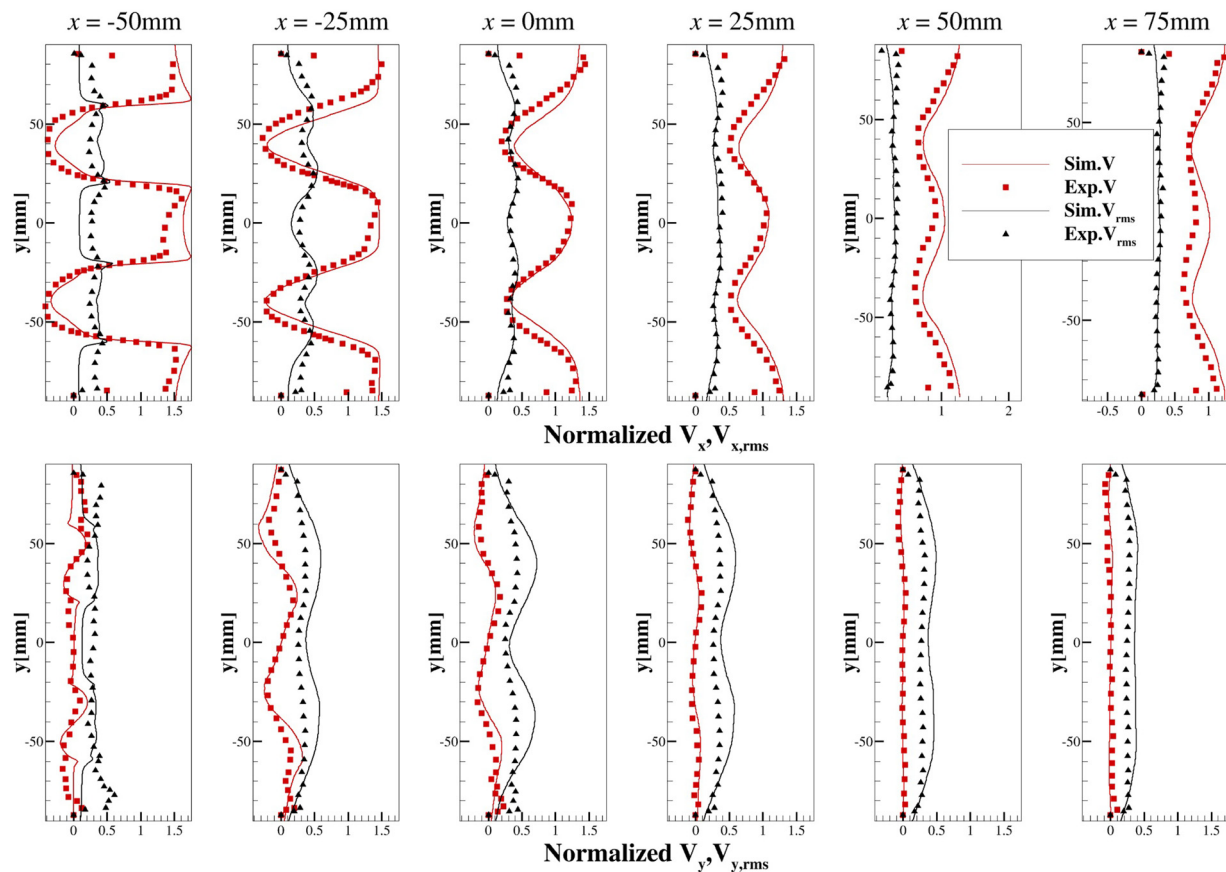

FIG. 5. The comparison of time-averaged and RMS axial and radial velocities between the experimental measurements (denoted as dots) and the simulation results (denoted as lines). The velocities are normalized by the inlet air velocity of 15.94 m/s.
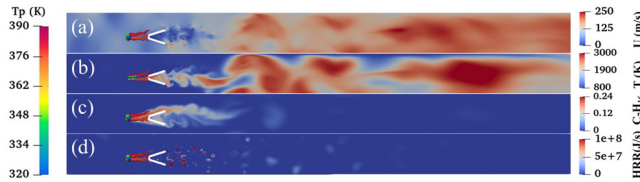
FIG. 6. The combustion snapshots in the upper half of the computational domain for (a) velocity, (b) temperature, (c) mass fraction of fuel, and (d) HRR.

results agree well with the experimental measurements. The two negative axial velocity peaks at $x = -50$ mm denote the recirculation zone. The slight discrepancy for radial velocities at $x = -50$ and -25 mm may be related to the measurement location that is close to the bluff-body leading to the measurement error. The pressure comparison is not performed in this work. A different but similar experiment with two bluff-bodies connected to each other has been conducted before. It shows that the order of magnitude is similar to the present simulation. The pressure comparison will be conducted in future work.

The combustion snapshots for the velocity, the temperature, the mass fraction of fuel, and the HRR in the upper half of the computational domain are shown in Fig. 6. It shows that the velocity increases significantly after the bluff-body at Fig. 6(a) due to the combustion expansion with high temperature at Fig. 6(b). The Kelvin–Helmholtz type instability shown in Figs. 6(a) and 6(b) appears downstream of the bluff-body. The liquid n-heptane fuel mainly evaporates before the bluff-body and the mass fraction of fuel extends to two times the distance of the bluff-body, which can be observed in Fig. 6(c). The high HRR in Fig. 6(d) concentrates in the region that is attached to the tail of the bluff-body. It implies that the fuel vapor and air mix well in this region leading to the stabilization of flame after the bluff-body.

B. Sample points and sensitivity analysis

Fourteen initial sample points are preset considering both the computational cost and the accuracy of the surrogate model. More sample points can be given to expedite the convergence of the optimization process, but it goes against the goal of this framework to quickly obtain the optimization points. The 14 sample points are obtained
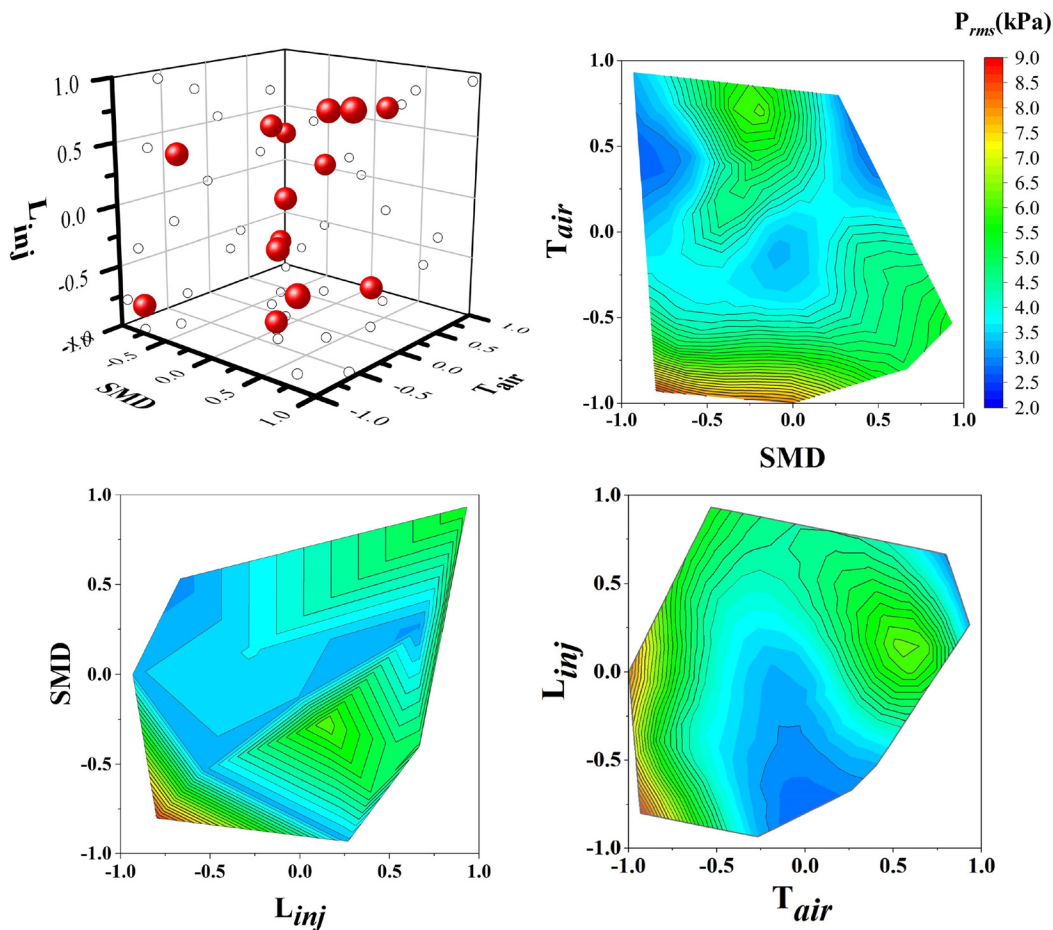

FIG. 7. (a) The sampling points with projection in three-dimensional $SMD - T_{air} - L_{inj}$ space. The sampling points are represented by red dots, and the projection points are represented by black circles. The projection of the sampling points to each two-dimensional space, including (b) $SMD - T_{air}$ space, (c) $L_{inj} - SMD$ space, and (d) $T_{air} - L_{inj}$ space.
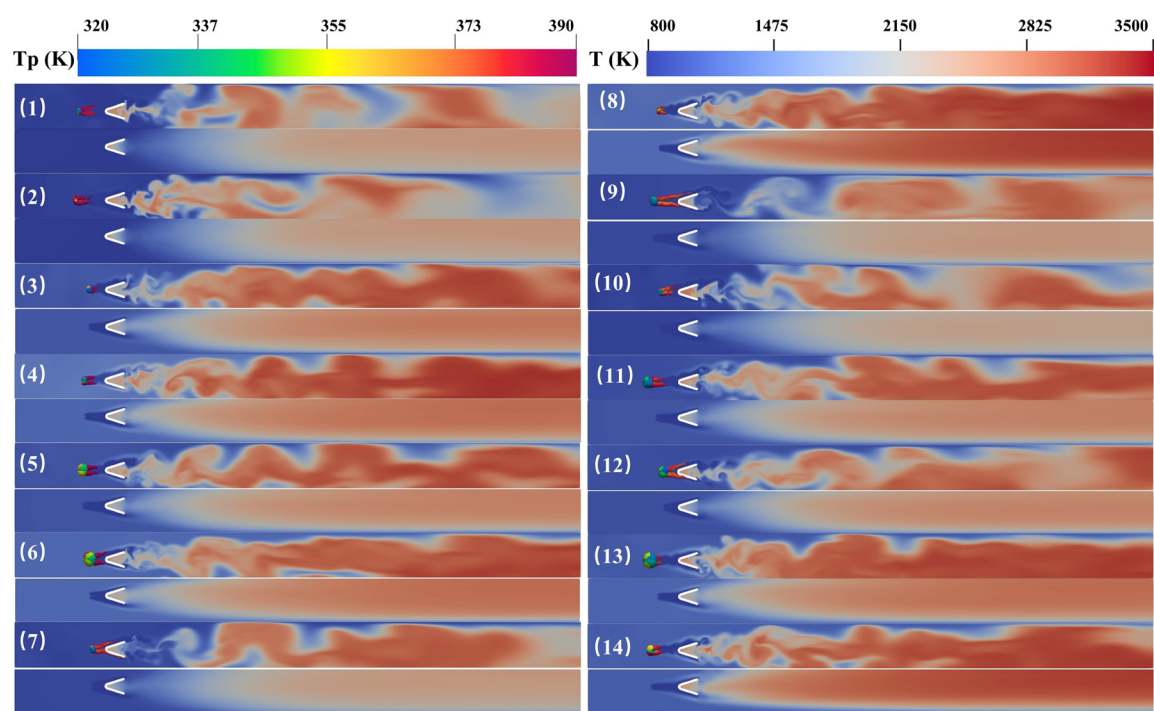
22 November 2025 03:01:10

FIG. 8. The instantaneous (upper panel) and time-averaged (lower panel) contours of temperature for the 14 sampling points. The liquid droplets are colored by droplet temperature in the upper panel.

using the Latin hypercube sampling (LHS) method, which is a widely used space-filling method[34] in multi-dimensional sampling issues. Compared to other sampling methods, the LHS method is designed to accurately reconstruct the design space with fewer iterations, which is more efficient. The overall sampling points in three-dimensional $SMD - T_{air} - L_{inj}$ space are shown in Fig. 7. The three coordinates are normalized to $[-1, 1]$. As shown in Fig. 7(a), the 14 sampling points occupy the whole three-dimensional space denoting the effectiveness of the Latin hypercube sampling process. Subsequently, the sampling points are projected onto each two-dimensional space, yielding the outcomes illustrated in Figs. 7(b)–7(d). It shows that P_{RMS} does not change linearly along a certain design variable, which also implies that these design variables have a significant influence on thermoacoustic stability.

Figure 8 shows the instantaneous and time-averaged contours of temperature for the 14 initial sampling points. The liquid droplets are colored by droplet temperature in the upper panel. It shows that the temperature contours have significant differences among different sampling points. It is also consistent with the finding in Fig. 7 that the three design variables have a significant influence on thermoacoustic stability.

To further assess the influence of the selected input variables on P_{RMS}, a comparative analysis is conducted between the maximum and minimum values of each input variable, as well as the baseline case. The results are shown in Table III. The results of samples 2 and 3 indicate that increasing the air preheating temperature significantly decreases P_{RMS}. When T_{air} increases, the evaporation process is enhanced and the instability is decreased.[22] The results of samples

4 and 5 indicate that P_{RMS} is first increased and then decreased with the increase in SMD. When SMD increases, atomization quality is decreased. However, it can be considered that moderately increasing SMD helps to decrease combustion instability. The results of samples 6 and 7 indicate that P_{RMS} is first decreased and then increased with the increase in L_{inj}. When L_{inj} increases, the evaporation distance and mixing with air are decreased, further affecting the phase relationship between fuel supply and heat release,[21] finally influencing the combustion instability.

Furthermore, Fig. 9 displays the sensitivity analysis results for each input variable and P_{RMS} based on the baseline case, which shows the relative significance of the selected input variables. It is evident that L_{inj} exhibits a positive influence on the increase in P_{RMS}, while SMD and T_{air} exhibit a negative influence, with T_{air} demonstrating the most pronounced effect.

TABLE III. Values of input variables and the objective for the baseline case as well as the samples for the sensitives analysis.

Number	T_{air}(K)	SMD (μm)	L_{inj} (mm)	P_{RMS} (Pa)
1	800	60	155	8062.137
2	1000	60	155	2886.008
3	1200	60	155	2271.048
4	800	20	155	6385.523
5	800	100	155	6684.069
6	800	60	133.8	8121.722
7	800	60	176.2	8915.085

FIG. 9. Sensitive analysis on the baseline case.

FIG. 11. The time-averaged contours of the baseline case (upper panel) and the optimal case (lower panel) for (a) velocity, (b) temperature, and (c) mass fraction of fuel.

C. Optimization results

Figure 10 shows the Bayesian optimization iteration results based on the baseline case and initial sampling points. Sample 0 denotes the baseline case, and samples 1–14 denote the initial sampling points. It shows that P_{RMS} of the optimization results denoted as the number 15 and 17 are smaller than all the sampling points, which implies the effectiveness of the Bayesian optimization process. It also shows that P_{RMS} of most sampling points is significantly smaller than the baseline case, implying that within the defined design space (Table I), the overall impact of the selected design variables tends to improve the combustion stability. The input parameters for the baseline case ($SMD = 60\,\mu m$, $T_{air} = 800\,K$, and $L_{inj} = 155\,mm$) and the optimized case ($SMD = 70.68\,\mu m$, $T_{air} = 1160\,K$, and $L_{inj} = 169.141\,mm$) are different. P_{RMS} value of the baseline case is 8.1 kPa, while the P_{RMS} value of the optimized case is 2.9 kPa. Hence, the P_{RMS} value can be reduced by approximately 64% for the optimized case compared to the baseline case. It will be a very good demonstration of the method by performing a close-to-optimum experiment. However, it is difficult or impossible to perform the experiment due to the limitation of equipment. The maximum of the air preheating temperature is 800 K, which is far from 1160 K, and SMD is difficult to accurately control for the present liquid fuel supply equipment. Alternatively, we intend to perform high-fidelity simulations with the three-dimensional configuration,
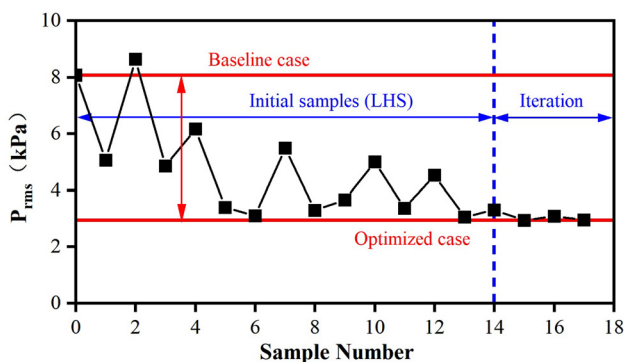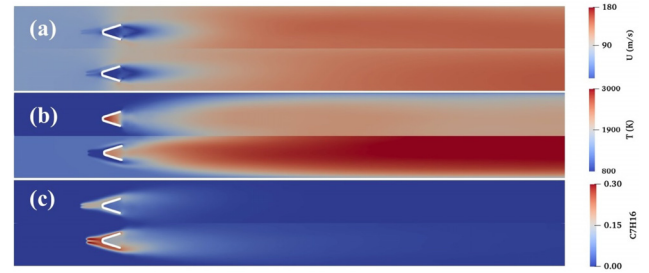
detailed reaction mechanism, and realistic boundary conditions for the baseline and the optimum cases. This will also be a feasible validation for the optimization framework.

Figure 11 shows the results of the optimized case compared to the baseline case. The velocity contour shows a similar trend between the baseline case and the optimized case. For the temperature contour, the optimized case shows a higher temperature overall, mainly because of an elevated initial temperature. The mass fraction and distribution of fuel also change significantly. For the former, it is because the optimized case has a higher air preheating temperature and leads to an increase in the evaporation process. For the latter, it is mainly because the location of liquid fuel injection is closer to the bluff-body for the optimized case, leading to a decrease in evaporation distance and mixing with air.

Figure 12 shows the temporal evolution of pressure values for the baseline and the optimized case. It shows a large mean pressure value attributed to the heat release of the spray combustion. It is also seen that pressure is stable after $t = 70\,ms$ for the baseline case and $t = 50\,ms$ for the optimized case. The P_{RMS} values for both cases are computed from 70 to 170 ms. Additionally, the pressure fluctuation for the optimized case is significantly smaller than the baseline case, which is consistent with the findings in Fig. 10. Until now, the Bayesian optimization process has achieved a satisfactory result in reducing pressure fluctuation.
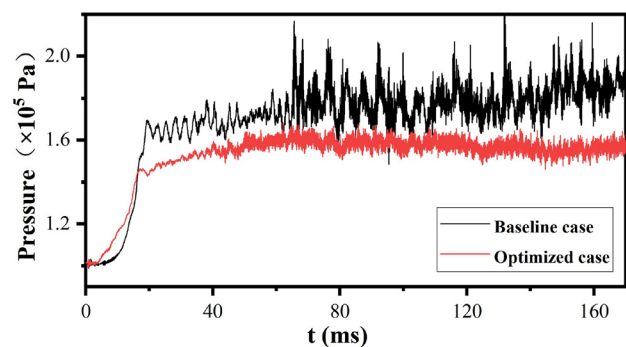
FIG. 10. The Bayesian optimization results based on the baseline case and initial sampling points.

FIG. 12. Temporal evolution of pressure values for the baseline (denoted as the black line) and the optimized case (denoted as the red line).

IV. CONCLUSIONS

This work provides a solution to the problem of optimizing the combustion instability of a bluff-body stabilized combustor. The OpenFOAM is employed for the simulation of spray combustion. The air preheating temperature, the Sauter mean diameter of fuel droplets, and the location of liquid fuel injection are regarded as input variables. The RMS of pressure amplitude is regarded as an optimization objective. The Bayesian optimization framework is proposed that includes the initial sampling process, constructing a surrogate model and sub-optimizing process for maximizing the acquisition function. It is found that P_{RMS} can be reduced by 64% for the optimized case compared to the baseline case. In future work, high-fidelity simulations with the three-dimensional configuration, detailed reaction mechanism, and realistic boundary conditions for the baseline and the optimum cases should be conducted. In addition, it would be worthwhile to develop a multi-objective framework that considers the NOx emission as an additional objective. Additionally, the impact of different surrogate models and acquisition functions should also be considered.

AUTHOR DECLARATIONS

Conflict of Interest

The authors have no conflicts to disclose.

Author Contributions

Jun Yang: Data curation (equal); Validation (equal); Visualization (equal); Writing – original draft (equal); Writing – review & editing (equal). **Changxiao Shao:** Conceptualization (equal); Funding acquisition (equal); Methodology (equal); Project administration (equal); Software (equal); Supervision (equal); Writing – original draft (equal); Writing – review & editing (equal). **Lei Wang:** Data curation (equal); Software (equal); Writing – original draft (equal); Writing – review & editing (equal). **Qizhe Wen:** Data curation (equal); Writing – original draft (equal). **Niewei Yang:** Data curation (equal); Visualization (equal). **Zhi X. Chen:** Supervision (equal); Writing – review & editing (equal). **Lei Li:** Supervision (equal); Writing – review & editing (equal). **Qiang An:** Supervision (equal); Writing – review & editing (equal). **Tai Jin:** Supervision (equal); Writing – review & editing (equal). **Kun Luo:** Supervision (equal); Writing – review & editing (equal).

DATA AVAILABILITY

The data that support the findings of this study are available from the corresponding author upon reasonable request.

REFERENCES

[1] N. Davis and G. Samuelsen, "Optimization of gas turbine combustor performance throughout the duty cycle," Symp. (Int.) Combust. **26**, 2819–2825 (1996).

[2] D. C. Kyritsis, B. Coriton, F. Faure, S. Roychoudhury, and A. Gomez, "Optimization of a catalytic combustor using electrosprayed liquid hydrocarbons for mesoscale power generation," Combust. Flame **139**, 77–89 (2004).

[3] J. A. S. O. S. Motsamai and J. P. Meyer, "Optimization of gas turbine combustor mixing for improved exit temperature profile," Heat Transfer Eng. **31**, 402–418 (2010).

[4] D. J. J. Toal, X. Zhang, A. J. Keane, C. Y. Lee, and M. Zedda, "The potential of a multifidelity approach to gas turbine combustor design optimization," J. Eng. Gas Turbines Power **143**, 051002 (2021).

[5] A. Fichera and A. Pagano, "Application of neural dynamic optimization to combustion-instability control," Appl. Energy **83**, 253–264 (2006).

[6] J. R. Seume, N. Vortmeyer, W. Krause, J. Hermann, C.-C. Hantschk, P. Zangl, S. Gleis, D. Vortmeyer, and A. Orthmann, "Application of active combustion instability control to a heavy duty gas turbine," J. Eng. Gas Turbines Power **120**, 721–726 (1998).

[7] Y. Liu, J. Tan, H. Li, Y. Hou, D. Zhang, and B. R. Noack, "Simultaneous control of combustion instabilities and NO_X emissions in a lean premixed flame using linear genetic programming," Combust. Flame **251**, 112716 (2023).

[8] J. Bell, M. Day, J. Goodman, R. Grout, and M. Morzfeld, "A Bayesian approach to calibrating hydrogen flame kinetics using many experiments and parameters," Combust. Flame **205**, 305–315 (2019).

[9] Q. Lin, C. Zou, S. Liu, Y. Wang, L. Lu, and C. Peng, "An improved 2-pentanone low to high-temperature kinetic model using Bayesian optimization algorithm," Combust. Flame **231**, 111453 (2021).

[10] Z. Zhou, C. Huang, K. Lin, Y. Wang, C. K. Law, and B. Yang, "High-efficiency design of combustion kinetic experiments based on genetic algorithm," Proc. Combust. Inst. **39**, 5219–5228 (2023).

[11] Y. Wang, C. Tao, Z. Zhou, K. Lin, C. K. Law, and B. Yang, "Clustering algorithm for experimental datasets using global sensitivity-based affinity propagation (GSAP)," Combust. Flame **259**, 113121 (2024).

[12] L. Cai, H. Pitsch, S. Y. Mohamed, V. Raman, J. Bugler, H. Curran, and S. M. Sarathy, "Optimized reaction mechanism rate rules for ignition of normal alkanes," Combust. Flame **173**, 468–482 (2016).

[13] T. A. Casey and H. N. Najm, "Estimating the joint distribution of rate parameters across multiple reactions in the absence of experimental data," Proc. Combust. Inst. **37**, 797–805 (2019).

[14] H. Chen, W. Ji, S. J. Cassady, A. M. Ferris, R. K. Hanson, and S. Deng, "Using shock tube species time-histories in Bayesian parameter estimation: Effective independent-data number and target selection," Proc. Combust. Inst. **39**, 5299–5308 (2023).

[15] G. D'Alessio, S. Sundaresan, and M. E. Mueller, "Automated and efficient local adaptive regression for principal component-based reduced-order modeling of turbulent reacting flows," Proc. Combust. Inst. **39**, 5249–5258 (2023).

[16] B. Shahriari, K. Swersky, Z. Wang, R. P. Adams, and N. de Freitas, "Taking the human out of the loop: A review of Bayesian optimization," Proc. IEEE **104**, 148–175 (2016).

[17] E. Brochu, V. M. Cora, and N. de Freitas, "A tutorial on Bayesian optimization of expensive cost functions, with application to active user modeling and hierarchical reinforcement learning," arXiv:1012.2599 (2010).

[18] K. Shimoyama, K. Sato, S. Jeong, and S. Obayashi, "Updating kriging surrogate models based on the hypervolume indicator in multi-objective optimization," J. Mech. Des. **135**, 094503 (2013).

[19] P. González-Tello, F. Camacho, J. Vicaria, and P. González, "A modified Nukiyama-Tanasawa distribution function and a Rosin-Rammler model for the particle-size-distribution analysis," Powder Technol. **186**, 278–281 (2008).

[20] H. Wang, K. Luo, and J. Fan, "Effects of turbulent intensity and droplet diameter on spray combustion using direct numerical simulation," Fuel **121**, 311–318 (2014).

[21] R. Desai and S. Chakravarthy, "Effect of fuel injection location on combustion instability in a dump combustor," AIAA Paper No. 2010-216, 2010.

[22]D. Cuppoletti, J. Kastner, J. Reed, and E. Gutmark, "High frequency combustion instabilities with radial V-gutter flameholders," AIAA Paper No. 2009-1176, 2009.

[23]J. C. Broda, S. Seo, R. J. Santoro, G. Shirhattikar, and V. Yang, "An experimental study of combustion dynamics of a premixed swirl injector," Symp. (Int.) Combust. **27**, 1849–1856 (1998).

[24]D. R. Jones, "A taxonomy of global optimization methods based on response surfaces," J. Global Optim. **21**, 345–383 (2001).

[25]N. Zhao, S. Jin, X. Shao, H. Zheng, and Y. Ren, "Effect of equivalence ratio on rotating detonation combustion with n-heptane sprays," Int. J. Hydrogen Energy **49**, 1009 (2023).

[26]S. Jeong, Y. Minemura, and S. Obayashi, "Optimization of combustion chamber for diesel engine using Kriging model," J. Fluid Sci. Technol. **1**, 138–146 (2006).

[27]O. Adeleke, S. Akinlabi, T.-C. Jen, P. A. Adedeji, and I. Dunmade, "Evolutionary-based neuro-fuzzy modelling of combustion enthalpy of municipal solid waste," Neural Comput. Appl. **34**, 7419–7436 (2022).

[28]T. Hong, H. Wang, W. Lin, and W. Lee, "Evolution of appropriate crossover and mutation operators in a genetic process," Appl. Intell. **16**, 7–17 (2002).

[29]R. Kumar and N. R. J. Hynes, "Prediction and optimization of surface roughness in thermal drilling using integrated ANFIS and GA approach," Eng. Sci. Technol., Int. J. **23**, 30–41 (2020).

[30]M. Gadalla, S. Karimkashi, I. Kabil, O. Kaario, T. Lu, and V. Vuorinen, "Embedded direct numerical simulation of ignition kernel evolution and flame initiation in dual-fuel spray assisted combustion," Combust. Flame **259**, 113172 (2024).

[31]A. Péquin, S. Iavarone, R. Malpica Galassi, and A. Parente, "The partially stirred reactor model for combustion closure in large eddy simulations: Physical principles, sub-models for the cell reacting fraction, and open challenges," Phys. Fluids **34**, 055122 (2022).

[32]S. Liu, J. C. Hewson, J. H. Chen, and H. Pitsch, "Effects of strain rate on high-pressure nonpremixed n-heptane autoignition in counterflow," Combust. Flame **137**, 320–339 (2004).

[33]Q. Meng, M. Zhao, H. Zheng, and H. Zhang, "Eulerian-Lagrangian modelling of rotating detonative combustion in partially pre-vaporized n-heptane sprays with hydrogen addition," Fuel **290**, 119808 (2021).

[34]M. D. McKay, R. J. Beckman, and W. J. Conover, "A comparison of three methods for selecting values of input variables in the analysis of output from a computer code," Technometrics **21**, 239–245 (1979).